Conventional *vs.* model-based measurement of patterned line widths from scanning electron microscopy profiles

Francesc Salvat-Pujol[a], John S. Villarrubia[b]

[a] *National Institute of Standards and Technology, Gaithersburg, MD 20899, USA*
Now at: CERN, CH-1211 Geneva 23, Switzerland
[b] *National Institute of Standards and Technology, Gaithersburg, MD 20899, USA*

Abstract

Scanning electron microscopy (SEM) is a practical tool to determine the dimensions of nanometer-scale features. Conventional width measurements use arbitrary criteria, e.g., a 50 % threshold crossing, to assign feature boundaries in the measured SEM intensity profile. To estimate the errors associated with such a procedure, we have simulated secondary electron signals from a suite of line shapes consisting of 30 nm tall silicon lines with varying sidewall angle and corner rounding. Four different inelastic scattering models were employed in Monte Carlo simulations of electron transport to compute secondary electron image intensity profiles for each of the shapes. The 4 models were combinations of dielectric function theory with either the single-pole approximation (SPA) or the full Penn algorithm (FPA), and either with or without Auger electron emission. Feature widths were determined either by the conventional threshold method or by the model-based library (MBL) method, which is a fit of the simulated profiles to the reference model (FPA + Auger). On the basis of these comparisons we estimate the error in the measured width of such features by the conventional procedure to be as much as several nanometers. A 1 nm difference in the size of, e.g., a nominally 10 nm transistor gate would substantially alter its electronic properties. Thus, the conventional measurements

*Corresponding author
Email address: john.villarrubia@nist.gov (John S. Villarrubia)

do not meet the contemporary requirements of the semiconductor industry. In contrast, MBL measurements employing models with varying accuracy differed one from another by less than 1 nm. Thus, a MBL measurement is preferable in the nanoscale domain.
Keywords: critical dimension (CD), inelastic scattering, JMONSEL, low-energy electron transport, nanometer scale dimensional metrology, SEM, simulation

---

1. Introduction

Electrons traversing a nanostructure pick up information about its shape, dimensions, and electronic properties [1]. In the preceding decades, electron microscopies have become increasingly sensitive to this information and have accordingly gained widespread use as practical tools to gain insight into the physical properties of material structures at the nanometer scale [2]. However, in order to reliably extract accurate information from the measured signal, a sound theoretical understanding of electron interactions in complex material geometries is often indispensable. Thus, the modeling of electron transport remains a topic of active development, both from a fundamental point of view and for a variety of contemporary applications in fields as varied as surface analysis and spectroscopies [3], surface tribology and chemical analysis of thin films [4], catalysis [5, 6], plasmonics, and nanoscale metrology [7, 8, 9], to name but a few.

In the present work we show by way of example how a dedicated effort in modelling cross sections for the inelastic scattering of low-energy electrons in a general-purpose Monte Carlo code for the simulation of electron transport proves fruitful and allows a state-of-the-art physics-based procedure to outperform an *ad hoc* and *de facto* industry-standard procedure for nanoscale dimensional analysis. For the sake of definiteness, we focus on the geometry depicted in the lower panel of Fig. 1, namely that of a Si line of 30 nm height and variable width, wall-tilt angle, and upper-corner curvature radius, resting on a flat substrate of

the same material. This geometry is relevant for the semiconductor industry: it describes, among others, key elements of modern FinFET transistors.

For such geometries, dimensional measurements consist in scanning a kilo-electronvolt electron beam across the line under investigation, thus obtaining its SEM intensity profile. The conventional approach to measure the linewidth from the acquired SEM signal relies on an *ad hoc* assignment of the position of the line edges, often taking the full width at half maximum (FWHM) of the measured profile as width of the line. From a practical point of view, this approach is certainly appealing: it is straightforward to implement, its computational cost is negligible, it is independent of the material composition and electronic properties of the patterned line, and it does not require detailed knowledge of electron transport through complex material geometries.

However, the conventional method described above suffers from an obvious source of uncertainty which renders it questionable for measurements at the nanometer scale: the position of the line edge does not result from physical considerations, but rather from an operational definition adopted by convention. Furthermore, the effect of other line parameters (height, wall-tilt angle, corner curvature radius, etc.) on the position of the edge is not accounted for. As shown below, the error incurred with such a measurement can easily approach 2 nm. This can be dismissed as nearly irrelevant for linewidths above a few 100 nm, but not for contemporary linewidths of 7 nm to 15 nm: indeed, variations by more than 1 nm in the fin width of a FinFET transistor lead to important changes in its effective capacitance and effective current [10]. For this reason, modern linewidth measurements need to be accurate within a fraction of 1 nm, that is, within a few interplanar distances in crystalline materials. Clearly, the conventional approach is not sufficiently accurate for these applications.

Given the lack of a standard against which to compare SEM linewidth measurements, an alternative approach is necessary to estimate the error incurred by the conventional measurement outlined above. A particularly fruitful approach consists in focusing efforts on understanding how the SEM signal arises on the basis of sound physical models. We have performed JMONSEL [7] Monte Carlo

simulations of electron transport, using the NIST Electron Elastic-Scattering Cross-Section Database (NIST-SRD64) for the elastic cross sections and for inelastic electron scattering in bulk media a semiclassical dielectric formalism description of inelastic electron collisions based on a state-of-the-art Full-Penn dielectric function extension model, the relevant aspects of which are outlined below. Note that we disregard surface plasmon excitations at the substrate surface and on the nanostructured lines. Under the assumption that our most realistic electron-transport model constitutes a sufficiently realistic description of the formation of the SEM signal, we have simulated linescan profiles for a battery of lines of known (chosen) width, wall-tilt angle, and corner curvature radii, taken as surrogates of actual SEM linescans. As shown below, the conventional linewidth measurement applied to our battery of simulated linescans revealed errors which do not meet the contemporary requirements of the semiconductor industry.

An alternative measurement approach has been developed [11, 7], consisting in generating a library of Monte-Carlo simulated linescans $I(\boldsymbol{p})$ using state-of-the-art interaction cross sections, for a dense mesh of various geometrical parameters $\boldsymbol{p}$ (*e. g.* line width, wall-tilt angle, top curvature radius, etc.), at a given primary energy for a given material. A nonlinear least-squares fit of the parameters $\boldsymbol{p}$ to an experimental (or, in this work, simulated) linescan $\tilde{I}$ yields a measurement of the geometrical properties of the actual line. In this work we examine the extent to which a model-based measurement incurs errors smaller than the conventional measurement outlined above, and whether the uncertainty required by the semiconductor industry (smaller than 1 nm) is attained. Villarrubia and Ding previously reported a similar exercise to determine the sensitivity of width determinations to model assumptions for a set of models [12]. The present comparison differs from the earlier one inasmuch as the earlier set of models did not include the industry conventional method, nor did it show the effects of the choice of dielectric-function model on the measured linewidth. In this work we compare the performance of an inelastic electron scattering model based on the single-pole approximation (SPA) *vs.* the full

Penn algorithm (FPA), both described below.

Note that our procedure only allows us to determine the sensitivity of the model-based procedure to the use of different dielectric-function models in the description of low-energy inelastic electron collisions in solids. Thus, our analysis based on those sensitivities estimates only model-associated uncertainty components and omits others associated with scan linearity, image noise, scale calibration, etc. Despite that the former is not the total uncertainty, it is nevertheless relevant to compare it to the measurement uncertainty required for semiconductor electronics or other relevant technological applications. Since additional error sources can only increase the total uncertainty, each of the components, including this one, must be smaller than the tolerance, and methods to drive down the uncertainty of each of those that initially exceed the tolerance are necessary. When referring to the model-based procedure, the term *measurement* will be used without further stress that the linescans to which it is applied in this work were obtained from a Monte Carlo simulation.

The article is structured as follows. In section 2 we provide a general overview of the employed electron transport model used to describe the formation of the SEM signal, focusing on the inelastic-scattering cross section. We discuss the shortcomings at low kinetic energies of the frequently used SPA, and how these are overcome by the use of the more realistic FPA. In section 3 we describe the combinations of line shapes and instrument parameters that were used to produce corresponding libraries of simulated linescans that were in turn used to assess the errors of conventional and model-based measurement procedures. In section 4 we discuss the error incurred when applying the conventional algorithm to measure the linewidth. In section 5 the physics-based measurement is outlined, and its uncertainties are discussed. The summary and conclusions of the work are presented in section 6.

2. Electron-transport model

In order to model how the SEM signal arises, simulations of sub-30-keV electron transport in complex solid geometries with state-of-the art transport models can be reliably carried out with the Monte Carlo simulation code JMONSEL (see [7] for a broader and more detailed account of the transport models implemented in JMONSEL). The relevant aspect of the electron transport model for the present work is the differential inelastic inverse mean free path for inelastic scattering of the projectile electron in the solid, given within the semiclassical dielectric formalism in Hartree atomic units by [13]

$$\frac{\mathrm{d}^2\lambda_i^{-1}}{\mathrm{d}\omega\mathrm{d}q} = \frac{2}{\pi v^2}\frac{1}{q}\mathrm{Im}\left[-\frac{1}{\varepsilon(q,\omega)}\right], \tag{1}$$

where ω is the energy loss of the projectile electron, q the modulus of the momentum transfer to a target electron, v the speed of the projectile electron, and $\varepsilon(q,\omega)$ the dielectric function of the material. The latter is often measured (or calculated ab initio) as a function of only ω; an extension to $q > 0$ is needed. Several extension algorithms have been developed in the past decades [13, 14, 15, 16, 17, 18, 19, 20, 21, 22], the most recently widespread being the so-called single-pole approximation (SPA) and the full-Penn algorithm (FPA). The SPA dielectric function model is given by

$$\mathrm{Im}\left[-\frac{1}{\varepsilon_{\mathrm{SPA}}(q,\omega)}\right] = \frac{1}{1+\dfrac{\pi q^2}{6k_F(\omega_0)}}\mathrm{Im}\left[\frac{-1}{\varepsilon(\omega_0)}\right], \tag{2}$$

where $\mathrm{Im}[-1/\varepsilon(\omega_0)]$ is the energy-loss function at $q = 0$, obtained experimentally or from ab initio calculations [23], ω_0 is a solution to the equation

$$x^3+a(q)x^2+b(q,\omega) = 0, \qquad a(q) = \frac{\pi^{2/3}}{2\ 6^{1/3}}q^2, \qquad b(q,\omega) = \frac{q^4}{4}-\omega^2, \qquad x = \omega_0^{2/3}, \tag{3}$$

and

$$k_F(\omega_p) = \left(\frac{3\pi}{4}\right)^{1/3}\omega_p^{2/3}, \tag{4}$$

where ω_p is the plasma frequency of an electron gas with the average density of electrons in the actual solid. Whereas the SPA includes only plasmon-like

response terms, the FPA is more realistic in that it additionally accounts for electron-hole excitations. We follow here Shinotsuka *et al.*'s implementation [13], given by

$$\mathrm{Im}\left[-\frac{1}{\varepsilon_{\mathrm{FPA}}(q,\omega)}\right] = \mathrm{Im}\left[-\frac{1}{\varepsilon(q,\omega)}\right]_{\mathrm{pl}} + \mathrm{Im}\left[-\frac{1}{\varepsilon(q,\omega)}\right]_{\mathrm{eh}}, \tag{5}$$

where

$$\mathrm{Im}\left[-\frac{1}{\varepsilon(q,\omega)}\right]_{\mathrm{pl}} = \pi g(\omega_0)\frac{1}{\left|\dfrac{\partial\varepsilon_1^L(q,\omega,\omega_p)}{\partial\omega_p}\right|_{\omega_p=\omega_0}}\Theta(q_m(\omega,\omega_0)-q), \tag{6}$$

with ω_0 the root of the equation

$$\varepsilon_1^L(q,\omega,\omega_0) = 0, \tag{7}$$

and

$$\mathrm{Im}\left[-\frac{1}{\varepsilon(q,\omega)}\right]_{\mathrm{eh}} = \int_0^\infty \mathrm{d}\omega_p\; g(\omega_p)\mathrm{Im}\left[-\frac{1}{\varepsilon^L(q,\omega,\omega_p)}\right]\Theta[q-q_m(\omega,\omega_p)]\Theta[q_p(\omega,\omega_p)-q], \tag{8}$$

where Θ is the Heaviside step function. Expressions for q_m, q_p, $g(\omega_0)$, and the Lindhard dielectric function $\varepsilon^L(q,\omega,\omega_p)$, with real and imaginary parts $\varepsilon_1^L(q,\omega,\omega_p)$ and $\varepsilon_2^L(q,\omega,\omega_p)$ respectively, are given in [13], including limiting expressions to avoid numerical issues. Implementation details and technicalities are presented in Appendix A.

We have also given a rough account of Auger electron emission. After an inner-shell ionization, a vacancy is left in an atomic shell. An electron from a more loosely bound shell can undergo a transition and fill the vacancy, whereupon the energy difference can either be released as a photon (fluorescence photon) or it can be invested in emitting an Auger electron. Atomic relaxation data from the Evaluated Atomic Data Library (EADL) of Perkins et al. [24] were used, as implemented in the PENELOPE 2014 [25] databases which, for a vacancy in a given shell, conveniently express the probability for each Auger transition and the energy of the emitted Auger electron. Once the corresponding Auger transition is selected, a secondary electron (the Auger electron) is

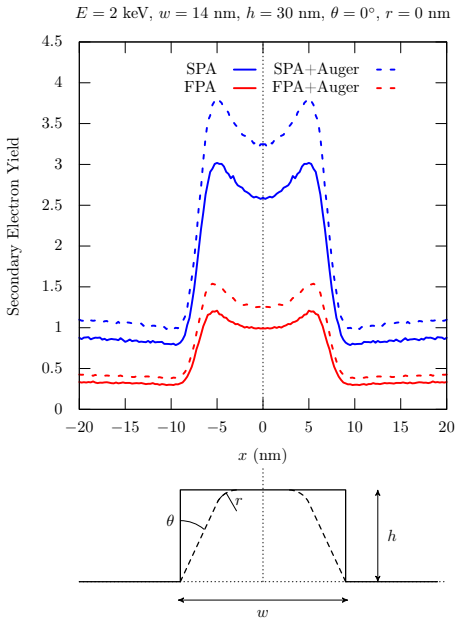

Figure 1: (Upper panel) Simulated linescans as a function of the position of the electron beam for the various models considered in this work and (lower panel) two examples of line geometry showing for the dashed curve the varied parameters: bottom linewidth w, wall-tilt angle θ, and curvature radius r. The line height h was not varied in this work. The linescans have been symmetrized around $x = 0$.

added to the stack. The vacancy left behind by the Auger electron is subsequently relaxed by iterating the process above. Note that we do not keep track of fluorescence photons because their long mean free path means electrons generated by them carry little topographic contrast. In the primary-energy domain considered below (200 eV to 10 keV), the inclusion of Auger-electron emission yields simulated linescans with an intensity enhanced by up to 20 % compared to linescans simulated without Auger emission (see *e. g.* upper panel of Fig. 1).

3. Library of simulated linescans

For each of the four models at our disposal, henceforth referred to as SPA, SPA with Auger emission (SPA+Auger), FPA, and FPA with Auger emission

(FPA+Auger), we have simulated a library of linescans $L_m(w_i, \theta_j, r_k; x, E)$ for Si lines on a Si substrate. The lines are 30 nm high, with

- bottom widths w_i from 8.5 nm to 15.5 nm in steps of 0.5 nm,
- wall-tilt angles θ_j from 0° to 3° in steps of 1°,
- top curvature radii r_k from 0 nm to 3 nm in steps of 1 nm.

40 000 primary electrons were simulated for every beam position x in every simulated linescan. The lower panel of Fig. 1 displays a schematic representation of the geometry. The linescans were simulated by rastering the simulated electron beam perpendicularly to the symmetry axis of the line, from a substrate position $x = -100$ nm to $x = -1.5w$ in steps of 1 nm, and in steps of 0.25 nm from $x = -1.5w$ to $x = 0$ nm (the center of the line), using a two-dimensional Gaussian beam profile with a standard deviation of 1 nm. Six primary energies E were considered, spanning the experimentally relevant energy domain: (200, 500, 1000, 2000, 5000, and 10 000) eV.

Figure 2 displays the variation of the simulated secondary electron yield for various E (panel a), w (panel b), θ (panel c), and r (panel d) for a particular model (FPA without Auger emission), with respect to a base case with $E_0 = 500$ eV, $w_0 = 10$ nm, $\theta_0 = 2°$, $r_0 = 2$ nm. The variation with energy (panel a) follows the energy dependence of the secondary electron yield in Si, which exhibits a maximum at a few hundred electronvolts and decreases monotonically for higher energies. The shape of the intensity edge, and not merely its amplitude and offset, vary with energy. For example, the edge bloom as measured by the ratio of maximum intensity near the edge to intensity at the line center ($x = 0$) decreases as the beam energy increases, as one would expect due to the increasing size of the interaction volume. As one increases the width (panel b) one sees the linescan extend as expected to values of x farther from $x = 0$, and the wider the line the lower the chance that secondary electrons have of emerging *e. g.* through the side walls, hence the decrease in the simulated intensity near the line center. A similar effect is expected as one varies the wall

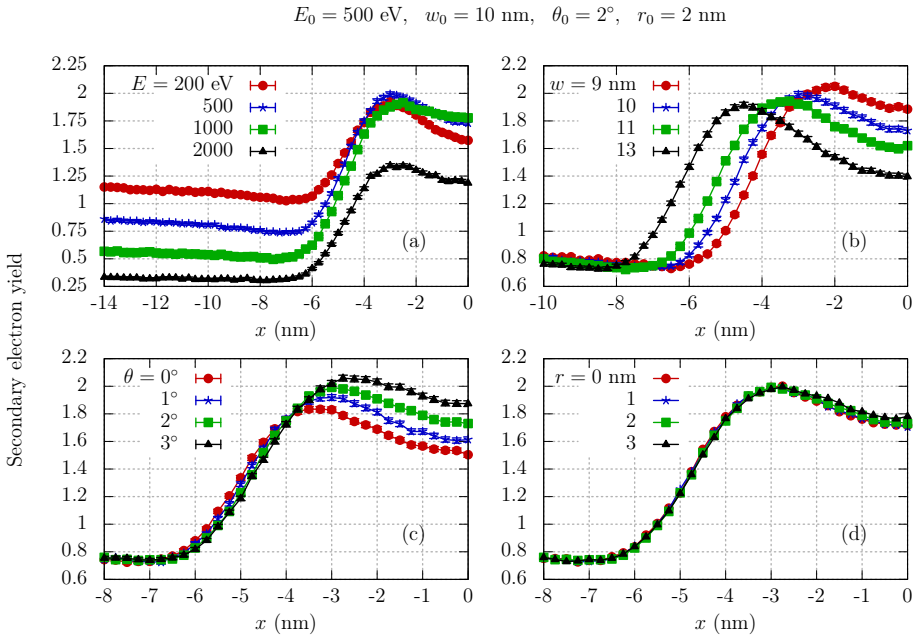

Figure 2: Variation of the linescans simulated with the FPA model (without Auger emission) as a function of the primary energy E (panel a), the bottom linewidth w (panel b), the wall tilt angle θ (panel c), and the curvature radius r (panel d) with respect to a reference case with $E_0 = 500$ eV, $w_0 = 10$ nm, $\theta_0 = 2°$, $r_0 = 2$ nm.

tilt-angle (panel c), where the more tilted the side angle the larger the chance that secondary electrons have of escaping the line. Finally, panel d displays the variation in the curvature radius r: the more curved the upper corner of the line, the larger is the chance that a secondary electron can make it out of the line. Owing to the small extent of the corner region relative to the line width, variations are subtle, and error bars are omitted to avoid obscuring them. We therefore anticipate that the curvature radius will be the most difficult of the considered parameters to extract from the model-based measurement outlined below.

The four generated linescan libraries (one per examined model) allow us to examine two questions. On the one hand, applying the conventional linewidth measurement to the simulated linescans and comparing with the actual width of the simulated line allows one to estimate the error incurred by the conventional measurement (section 4). On the other hand, taking linescans from our most refined model (FPA with Auger emission) as surrogates for actual measurements[1], we can use less refined linescan libraries (SPA, SPA with Auger, and FPA) to fit the "measurements" and compare the fitted widths with the actual widths. This allows us to estimate the sensitivity of the model-based measurement to approximations or simplifications of the model (section 5).

4. Error incurred in conventional linewidth measurements

Given an experimental (or simulated) linescan, *e. g.* the ones shown in the upper panel of Fig. 1, the linewidth is given by the difference between right and left edge positions, $x_{\text{right}} - x_{\text{left}}$. The conventional approach to determine x_{right} consists, within minor variations, in:

1. Determining an average baseline value y_{min} to the right of the center of the line. This is preferred to taking the minimum of the linescan, because

[1]Taking our detailed simulations as the reference has the advantage that we know all of the shape parameters precisely, which is not the case for measured linescans.

the latter is often shallow and very variable, and therefore difficult to determine systematically. Thus, one takes the average of the baseline intensity far away from the line minimum (say a multiple of the line height away). We have averaged the baseline from 70 nm to 100 nm away from the center of the line.

2. Determining the position $x_{\max}$ and intensity $y_{\max}$ of the profile maximum to the right of the center of the line.
3. Determining the abscissa x_{right} such that the profile intensity is $(y_{\max} + y_{\min})/2$.

One repeats steps 1 through 3 on the left side to determine x_{left}.

An estimate of the error incurred when measuring the linewidth with the conventional method outlined above can be readily obtained by applying the procedure to a library of linescans (for which the width is known precisely) simulated with our most refined electron-transport model (FPA with Auger-electron emission). Figure 3 displays the incurred error (the measured linewidth minus the actual width of the simulated linescan) as a function of the width used in the simulation for various primary energies, wall-tilt angles, and curvature radii. One clearly sees that the error incurred by the conventional measurement is largest (approaching 2 nm) at low primary energies. This error has low sensitivity to the curvature radius in the examined range. (Results for different radii, coded by the 4 plot marker shapes, lie almost on top of each other except in the leftmost, lowest energy panel.) On the other hand, the error is very sensitive to the wall-tilt angle. Whereas at low primary energies (below 1 keV) the smallest error is obtained for the smallest wall-tilt angle (0°, red markers), at somewhat higher energies the intermediate wall-tilt angles (1° and 2°, blue and green markers) result in a smaller error.

Thus, our analysis suggests that the error incurred when applying the conventional linewidth measurement can easily approach 2 nm for the lowest primary energy we have considered (200 eV). Whereas this is typically not a concern for linewidths above several tens of nanometers, in the sub-10-nm domain

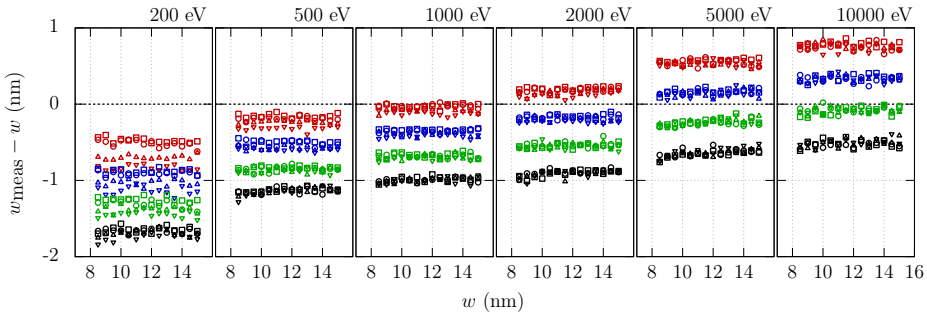

Figure 3: Overview of the error incurred when applying the conventional measurement to a library of linescans (including all considered primary energies, wall-tilt angles and curvature radii) simulated with our most refined model (FPA with Auger electron emission). Included are various energies (from left-most to right-most column: 200 eV, 500 eV, 1 keV, 2 keV, 5 keV, 10 keV), wall-tilt angles (0° in red, 1° in blue, 2° in green, 3° in black), and curvature radii (0 nm in squares, 1 nm in circles, 2 nm as triangles pointing up, and 3 nm as triangles pointing down).

variations of 1 nm in the linewidth lead to significantly different electronic properties and, thus, width measurement errors are required to be smaller than 1 nm [10]. Thus, the application of a conventional linewidth measurement becomes increasingly questionable for linewidths below a few 10s of nanometers.

5. Error incurred in model-based linewidth measurements

In this section we discuss the error incurred by a model-based linewidth measurement and compare it to that of the foregoing conventional measurement. As discussed in section 3, for each of our "crude" models $m = \{$SPA without Auger emission, SPA with Auger emission, and FPA without Auger emission$\}$, a library of linescans $L_m(w_i, \theta_j, r_k; x, E)$ was generated as a function of the position x away from the line symmetry axis, spanning widths w_i from 8.5 nm to 15.5 nm in steps of 0.5 nm, wall-tilt angles θ_j from 0° to 3° in steps of 1°, and top curvature radii r_k from 0 nm to 3 nm in steps of 1 nm, for various energies $E = \{200, 500, 1000, 2000, 5000, 10\,000\}$ eV. For each of these libraries, an interpolation function $I_m(w, \theta, r; x, E)$ was determined.

Three different model-based linewidth measurements [7] resulted from fitting to our refined-model (FPA with Auger emission) linescans $L(w_i, \theta_j, r_k; x, E)$ a model function $a + bI_m(w, \theta, r; E, x)$, where m runs over the three aforementioned coarser models, a and b are respectively the offset and scale parameter, taking as fit parameters $\{a, b, w, \theta, r\}$, considering that the beam energy E is known, and including the full linescan in $x \in [-100, 0]$ nm. This fit was done for all three of our coarser models, thus yielding three model-based estimates of the width for a broad range of line geometries, and allowing us to examine the sensitivity of the model-based measurement to the particularly important choice of dielectric-function model extension algorithm and to the absence of Auger-electron emission in the model. As we did for the conventional measurement algorithm in the previous section, we now consider the error in the model-based measurement of the linewidth, which is given by $w_{\text{meas}} - w$, where w_{meas} is the measured (fitted) width, and w is the actual width at which the refined-model linescan was simulated.

Figures 4 through 6 display, as a function of the width of the linescan simulated with our most refined model (FPA with Auger emission), the error incurred by the model-based measurement taking as input models the three available for our analysis, in increasing degree of realism: SPA without Auger emission, SPA with Auger emission, and FPA without Auger emission, respectively. The figures are further resolved with respect to the primary energy, wall-tilt angle, and curvature radius.

For all three model-based measurements, the error drops to a fraction of 1 nm. The error incurred by the SPA model (coarsest of the four examined here), displayed in Fig. 4, drops to roughly 0.5 nm at the lowest energy considered (200 eV), and can reach 1 nm at the highest energy considered (10 keV). Comparing the errors incurred by the SPA model (Fig. 4) with those incurred by the SPA model with Auger emission (Fig. 5), we see that switching Auger emission on or off does not lead to an observable reduction of the measurement error: the error incurred by using the comparatively coarse SPA model to fit FPA+Auger linescan widths prevails. Progressing from a coarse SPA model to

the FPA model (more realistic for slow secondary electrons) the error, displayed in Fig. 6, drops from $\approx 0.5\,\mathrm{nm}$ to $\approx 0.25\,\mathrm{nm}$, that is, to a distance comparable to the typical distance between atomic planes in a crystal.

Considering that the SPA model predicts considerably higher SE yields at low beam energies, it is interesting that the effect on the determined dimension was so small. We believe this is because our lines and substrate are of the same composition. Much of the yield difference is uniform and does not produce a significant change in the fitted size. There is no guarantee the same would be true for samples with material contrast in addition to topographic contrast.

As a measure of our intrinsic fitting error (due, e.g., to noise in our Monte Carlo simulations) we simulated linescans and fit them using libraries generated with the same model. In the worst case (beam energy of 10 keV) the mean and standard deviation of the error were $0.0005 \pm 0.01\,\mathrm{nm}$. This is negligible even with respect to the small differences ($\approx 0.25\,\mathrm{nm}$) we observe between models

Whereas the conventional measurement yielded errors which could easily approach 2 nm, the estimated error incurred by the model-based measurement drops to a fraction of 1 nm, thus complying with the expectations of the semiconductor industry (accuracy better than 1 nm). Although in this work we have focused only on the uncertainty due to model choices, it should be noted that further components may contribute to the uncertainty in the measured linewidth: scan linearity, image noise, scale calibration, etc. Each of these must be below 1 nm, such that their combination also remains below this threshold as expected by the semiconductor industry.

For the results shown in Figs. 3 through 6, the beam was Gaussian with standard deviation fixed at $\sigma = 1$ nm. This value was chosen because it is close to the value observed in earlier work with a high-resolution SEM in our laboratory.[7] We for this reason regard it (and the results) as representative of what should be attainable in practice. However, the beam size is seldom known exactly, and it is interesting to ask how a different beam size would affect our conclusions. To this end, we took a representative set of lines at primary energies (200, 500, 2000, and 5000) eV, included all considered wall-tilt angles and

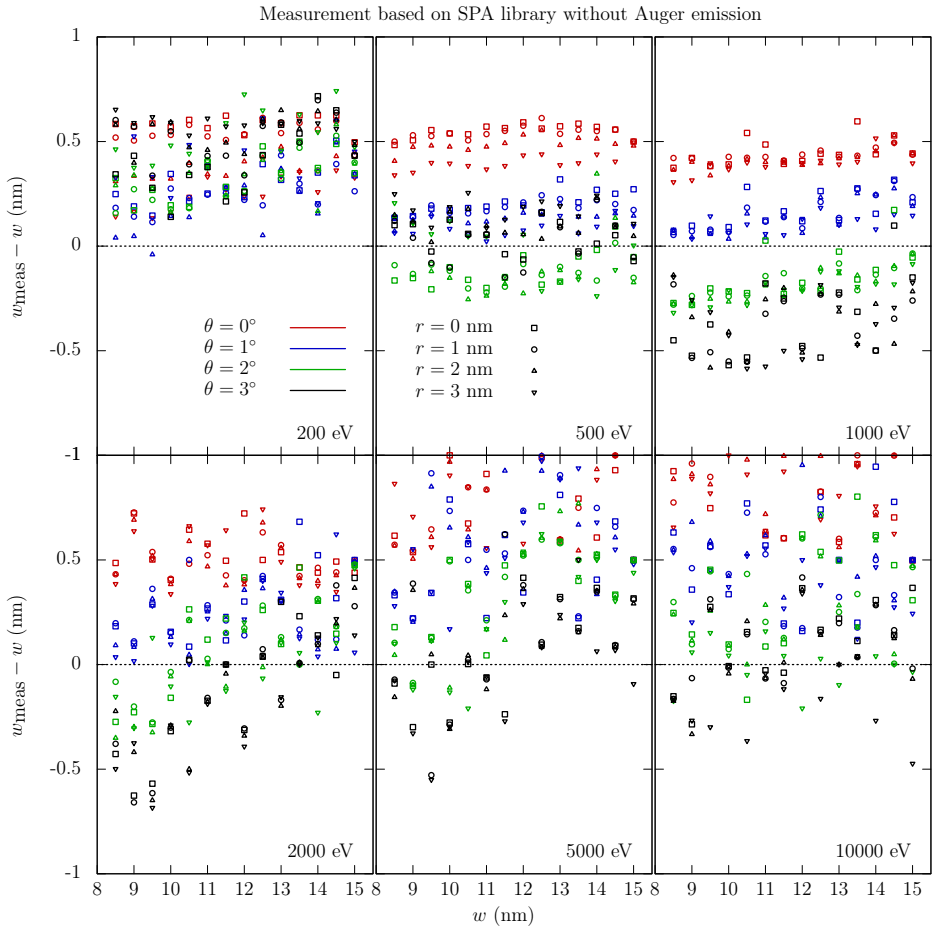

Figure 4: Error induced in measuring linescans generated with FPA+Auger with a model-based measurement relying on a library of linescans generated with a coarser model (SPA without Auger emission). Each of the panels corresponds to the indicated primary electron energies (from 200 eV to 10 keV). Wall-tilt angles $0°, 1°, 2°, 3°$ are coded in red, blue, green, and black, respectively. Curvature radii 0 nm, 1 nm, 2 nm, and 3 nm, are coded as empty squares, circles, upward pointing and downward pointing triangles, respectively.

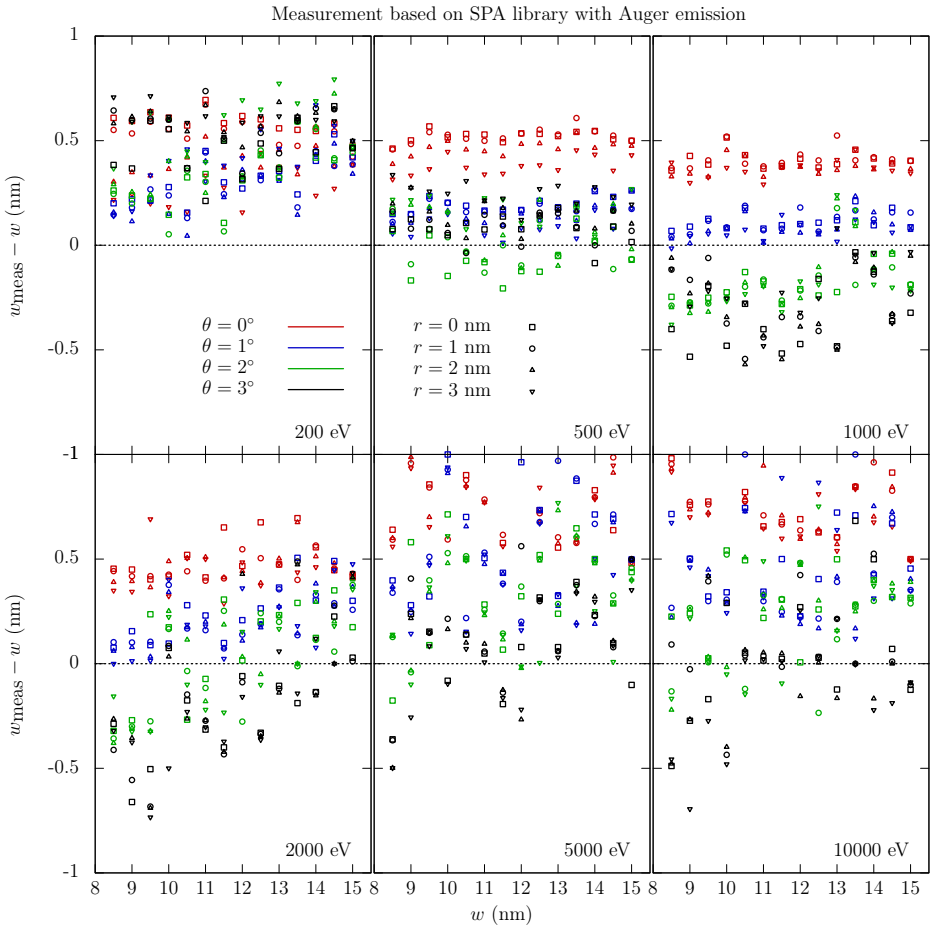

Figure 5: Same as Fig. 4 for a library of linescans generated with a coarser model (SPA with Auger emission).

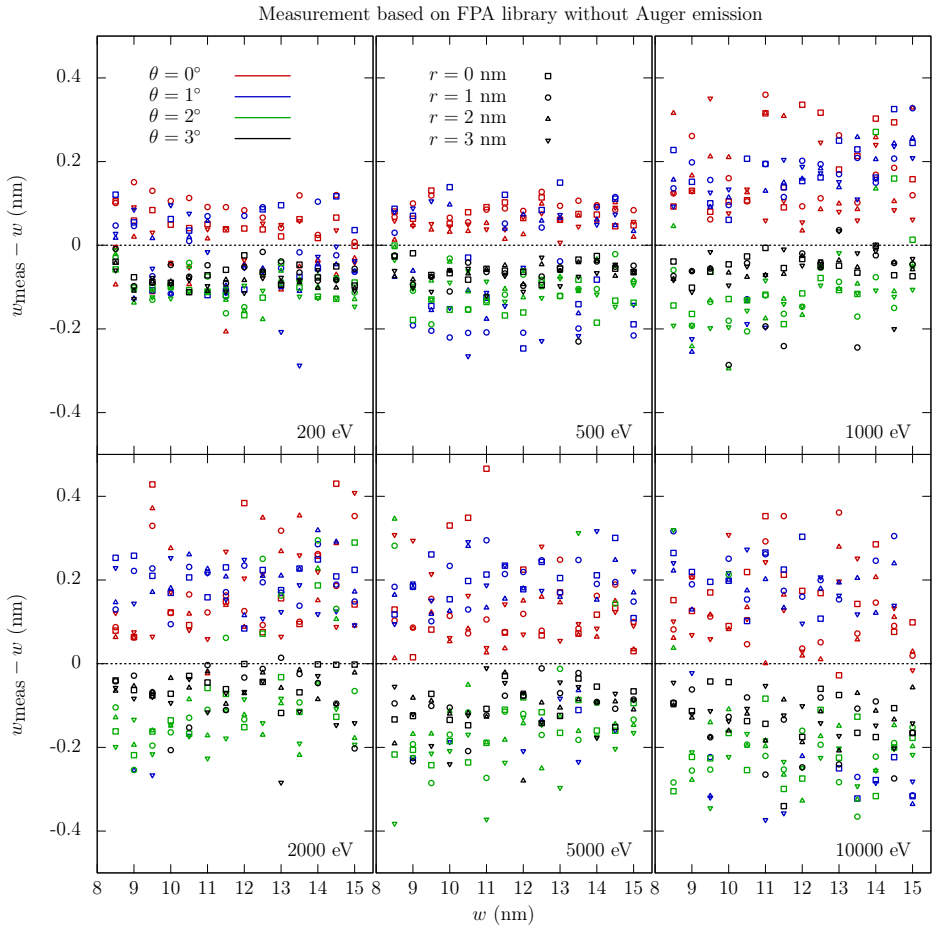

Figure 6: Same as Fig. 4 for a library of linescans generated with a coarser model (FPA without Auger emission). Note the change of scale in the ordinates with respect to the previous figures.

curvature radii, included widths of (8, 10, and 12) nm and convolved them with a Gaussian with 1.75 nm standard deviation. The beam standard deviation was thereby augmented to $\sqrt{(1\text{ nm})^2 + (1.75\text{ nm})^2} \approx 2.0$nm. We likewise extended our FPA+Auger linescan library, convolving it with Gaussians with standard deviations ranging from 0.75 nm to 2.25 nm in steps of 0.25 nm. This augmentation of the library permitted the fit procedure to also determine the beam size. With this setup, we have performed both a conventional measurement and a "beamsize-extended" model-based measurement on the representative set of lines described above. Whereas the conventional measurement led to errors reaching and exceeding 2 nm, the errors incurred by the beamsize-extended model-based measurement remained within 0.5 nm. Thus, as spot sizes were increased beyond those typical of our high-resolution SEM, errors in both the conventional and model-based width determinations increased, but those with the conventional method increased more than those with the model-based one, thereby strengthening the accuracy advantage of the latter. This is not surprising, given that the model-based method estimates the beam size based on the fit to features of the intensity profile whereas the conventional method has no means to distinguish changes due to beam size from those due to true changes in feature width.

6. Summary

In this work we have considered the problem of SEM width measurements of lines patterned in Si on a Si substrate. In general there are many possible sources of uncertainty in such a measurement, including scan linearity, image noise, scale calibration, etc. Most of these can be estimated by the usual methods: reversal, repeatability, etc. Errors due to the choice of model in the inelastic electron scattering description may be important but are not accessible by these techniques. In this work, we have concentrated on these model-associated uncertainties by comparing conventional and model-based determinations of widths on simulated SEM scans of a set of lines covering a range of shapes and sizes. The line di-

mensions were 30 nm height, width varying from 8.5 nm to 15.5 nm, sidewall angle from 0° to 3° and corner rounding from 0 nm to 3 nm. The conventional measurement procedure relies upon edge positions assigned by intensity threshold crossings in the SEM secondary electron image. We used state-of-the-art modeling of low-energy electron energy losses in a general-purpose Monte Carlo code to simulate intensity profiles across lines of known width and shape in such images. The conventional measurement procedure applied to the simulated profiles exhibited bias of up to almost 2 nm. These errors have significant dependence upon the sample's shape and the beam energy. The shape in particular is generally not known independently of the measurement, rendering such errors difficult to correct. We also compared model-based measurements using three models that were in varying degrees more primitive than our best model. Widths determined by the model-based measurements were less sensitive to changes in edge shape or beam energy than were the conventionally determined ones. Under the assumption that our most detailed electron-transport model provides a sufficiently realistic description of how the SEM signal arises, our analyses suggest that the error incurred even in model-based measurements with the more primitive models drops to a fraction of 1 nm, thus showing that efforts invested in further careful modeling of electron transport would prove fruitful for contemporary metrology applications. The illustrative example chosen for these simulations was drawn from semiconductor electronics, but we expect similar results for other applications where nanometer-scale accuracy is important, such as for nanoparticles, photonic devices, and nanotechnology.

Acknowledgement

F.S.-P. gratefully acknowledges funding by the NIST Guest Researcher Program. We are greatly indebted to Prof. Francesc Salvat from the *Universitat de Barcelona* for frequent discussions.

Appendix A. Implementation aspects

When implementing the FPA extension algorithm, one stumbles upon implementation issues that are seldom mentioned. The first of these concerns finding the root ω_0 of Eq. (7). We have proceeded by first attempting Brent's method [26] in the interval $\omega \in \left[10^{-5}, \min\left(\omega, \left|\frac{q}{2} - \frac{w}{q}\right|\right)\right]$, defaulting to the secant method if Brent's method cannot be started (no sign change between endpoints of the initial interval).

The evaluation of the FPA is computationally intensive. In particular, a tailored numerical-integration scheme is needed to evaluate Eq. (8). One approach to make calculations in a reasonable time consists in evaluating $\mathrm{Im}[-1/\varepsilon(q,\omega)]$ on a reasonably chosen grid of q and ω and using a quick integration scheme on these tabular abscissas, *e. g.*, the integral of the linear log-log interpolant. This, of course, assumes a dense enough grid, such that interpolation inaccuracies are palliated to the extent possible. In what follows, "interpolation" implies a linear log-log interpolation; similarly, "integration" implies the integral of the linear log-log interpolant.

We consider the following scheme:

- Given a table containing $\mathrm{Im}[-1/\varepsilon(\omega)]$ (or optical constants from which this quantity can be built), we extrapolate from the first two tabular abscissas to very small ω, say $\omega \approx \Delta E_{\mathrm{gap}} + 10^{-4}$ eV, where ΔE_{gap} is the band gap, so as to have also tabular abscissas along q for very small energy losses. This reduces integration errors for quantities at very low primary energies (where the energy-loss domain is very narrow and therefore with potentially few points and potentially large interpolation inaccuracies, a situation for which we try to compensate by adding more ω-abscissas).

- Similarly, in order to obtain an inelastic mean free path well resolved in energy, it is convenient to add relatively densely spaced ω-abscissas immediately above the Fermi energy.

- For each tabular ω-abscissa in the (augmented) optical data, we adap-

tively evaluate $\mathrm{Im}[-1/\varepsilon(q,\omega)]$ along $Q = q^2/2$, adding more Q abscissas wherever the curvature (absolute value of the relative difference between the i-th tabular value and the interpolation from the $(i-1)$-st and $(i+1)$-st points at the i-th tabular value) is largest. We make sure to add the point $\omega = q^2/2$, which corresponds to the maximum on the Bethe ridge, particularly relevant for large ω. We start with ≈ 200 equispaced points and add ≈ 300 adaptive abscissas, which proved to be reasonable.

- At this point we have different q abscissas for different ω. Thus, the resulting grid is not rectangular.

- The (usually very sharp) peak of $\mathrm{Im}[-1/\varepsilon(q,\omega)]$ along q shifts as ω varies. For ω-abscissas that are not close enough, this peak shift leads to interpolation artifacts at intermediate points. To palliate such potential errors, we add ≈ 100 abscissas in ω adaptively, wherever the peak shift along ω relative to the peak width along q is largest.

- Finally, as a precaution to minimize the impact of "wiggle"-artifacts in the cubic interpolation used in JMONSEL, we add further ω abscissas wherever the spacing in consecutive ω abscissas suddenly becomes larger by more than a factor of two.

- When calculating electronic-stopping properties, both the grid of primary energies and the grid of energy losses will be the grid of ω we generated as described above.

- When calculating the energy loss distribution $\mathrm{d}\lambda_i^{-1}(K,\omega)/\mathrm{d}\omega$, where K is the kinetic energy of the projectile electron, there is a minimum and a maximum energy loss, none of which will necessarily coincide with a tabular ω. Thus, when calculating

$$\lambda_i^{-1}(K) = \int_{\omega_{\min}(K)}^{\omega_{\max}(K)} \mathrm{d}\omega \, \frac{\mathrm{d}\lambda_i^{-1}(K,\omega)}{\mathrm{d}\omega} \tag{A.1}$$

or higher ω moments with our linear-log-log integration, one could miss the interval from $\omega_{\min}$ to the first tabular abscissa verifying $\omega \geq \omega_{\min}$

(and similarly for the upper integration bound). Thus, care should be taken to consider the value of the integrand at the tabular ω immediately below $\omega_{\min}$ for the purposes of this integral. If this is not observed, $\lambda_i(K)$ exhibits a sawtooth artifact for values of K immediately above the Fermi energy.

- The linear-log-log integration scheme above allows one to also calculate higher moments of the energy-loss distribution, such as the stopping power (average energy loss per unit path length),

$$S(K) = \int_{\omega_{\min}(K)}^{\omega_{\max}(K)} \mathrm{d}\omega\ \omega \frac{\mathrm{d}\lambda_i^{-1}(K,\omega)}{\mathrm{d}\omega}, \tag{A.2}$$

and the straggling parameter (related to the spread per unit path length of the energy distribution of an originally monochromatic beam of energy K),

$$\Omega^2(K) = \int_{\omega_{\min}(K)}^{\omega_{\max}(K)} \mathrm{d}\omega\ \omega^2 \frac{\mathrm{d}\lambda_i^{-1}(K,\omega)}{\mathrm{d}\omega}. \tag{A.3}$$

References

[1] F. J. García de Abajo, Optical excitations in electron microscopy, Rev. Mod. Phys. 82 (2010) 209–275.

[2] J. Nelayah, M. Kociak, O. Stephan, F. J. García de Abajo, M. Tencé, L. Henrard, D. Taverna, I. Pastoriza-Santos, L. M. Liz-Marzán, C. Colliex, Mapping surface plasmons on a single metallic nanoparticle, Nature 3 (2007) 348–353.

[3] L. C. Ann, S. Mahmud, S. K. M. Bakhori, Electron spectroscopy imaging and surface defect configuration of zinc oxide nanostructures under different annealing ambient, Appl. Surf. Sci. 265 (2013) 137–144.

[4] A. Tomala, A. Karpinska, W. S. M. Werner, A. Olver, H. Störi, Tribological properties of additives for water-based lubricants, Wear 269 (2010) 804–810.

[5] M. Setvín, U. Aschauer, P. Schreiber, Y. F. Li, W. Hou, M. Schmid, A. Selloni, U. Diebold, Reaction of O_2 with Subsurface Oxygen Vacancies in TiO_2 Anatase (101), Science 341 (2013) 988–991.

[6] M. Setvín, J. Hulva, H. Wang, T. Simschitz, M. Schmid, G. S. Parkinson, C. di Valentin, A. Selloni, U. Diebold, Formaldehyde Adsorption on the Anatase TiO_2(101) Surface: Experimental and Theoretical Investigation, J. Phys. Chem. C 121 (2017) 8914–8922.

[7] J. S. Villarrubia, A. E. Vladár, B. Ming, R. J. Kline, D. F. Sunday, J. S. Chawla, S. List, Scanning electron microscope measurement of width and shape of 10 nm patterned lines using a JMONSEL-modeled library, Ultramicroscopy 154 (2015) 15–28.

[8] C. J. Powell, W. S. M. Werner, H. Kalbe, A. G. Shard, D. G. Castner, Comparisons of Analytical Approaches for Determining Shell Thicknesses of Core-Shell Nanoparticles by X-ray Photoelectron Spectroscopy, J. Phys. Chem. C 122 (7) (2018) 4073–4082.

[9] J. A. Liddle, B. D. Hoskins, A. E. Vladar, J. S. Villarrubia, Research Update: Electron beam-based metrology after CMOS, APL Mater. 6 (7) (2018) 070701.

[10] P. Zeitzoff, K. Akarvardar, J. Mody, A. Konar, Metrology requirements and challenges for advanced FinFET technology: Insight from TCAD simulations, in: 2017 International Conference on Frontiers of Characterization and Metrology for Nanoelectronics, 2017, pp. 31–33.

[11] J. S. Villarrubia, A. E. Vladár, M. T. Potsek, Scanning electron microscope dimensional metrology using a model-based library, Surf. Interface Anal. 37 (2005) 951–958.

[12] J. S. Villarrubia, Z. J. Ding, Sensitivity of scanning electron microscope width measurements to model assumptions, J. Micro/Nanolith. MEMS MOEMS 8 (3) (2009) 033003.

[13] H. Shinotsuka, S. Tanuma, C. J. Powell, D. R. Penn, Calculations of electron inelastic mean free paths. X. Data for 41 elemental solids over the 50 eV to 200 keV range with the relativistic full Penn algorithm, Surf. Interface Anal. 47 (2015) 871–888.

[14] J. Lindhard, On the properties of a gas of charged particles, Mat. Fys. Medd. Dan. Vid. 28 (8) (1954) 1–57.

[15] N. D. Mermin, Lindhard dielectric function in the relaxation-time approximation, Phys. Rev. B 1 (5) (1970) 2362–2363.

[16] D. R. Penn, Electron mean-free-path calculations using a model dielectric function, Phys. Rev. B 35 (2) (1987) 482–486.

[17] J. M. Fernández-Varea, D. Liljequist, R. Mayol, F. Salvat, Calculation of inelastic mean free path and stopping power for electrons in solids from an optical-data model, USIP Report 92-06 (1992) 1–27.

[18] J. M. Fernández-Varea, R. Mayol, D. Liljequist, F. Salvat, Inelastic scattering of electrons in solids from a generalized oscillator strength model using optical and photoelectric data, J. Phys.-Condens. Mat. 5 (1993) 3593–3610.

[19] G. S. Atwal, N. W. Ashcroft, Relaxation of an electron system: Conserving approximation, Phys. Rev. B 65 (2002) 115109.

[20] J. M. Fernández-Varea, F. Salvat, M. Dingfelder, D. Liljequist, A relativistic optica-data model for inelastic scattering of electrons and positrons in condensed matter, Nucl. Instrum. Meth. B 229 (2005) 187–218.

[21] S. Tanuma, C. J. Powell, D. R. Penn, Calculations of electron inelastic mean free paths. IX. Data for 41 elemental solids over the 50 eV to 30 keV range, Surf. Interface Anal. 43 (2011) 689–713.

[22] H. Shinotsuka, S. Tanuma, C. J. Powell, D. R. Penn, Calculations of electron stopping powers for 41 elemental solids over the 50 eV to 30 keV range with the full Penn algorithm, Nucl. Instrum. Meth. B 270 (2012) 75–92.

[23] W. S. M. Werner, K. Glantschnig, C. Ambrosch-Draxl, Optical constants and inelastic electron-scattering data for 17 elemental metals, J. Phys. Chem. Ref. Data 38 (4) (2009) 1013–1092.

[24] S. T. Perkins, D. E. Cullen, M. H. Chen, J. H. Hubbell, J. Rathkopf, J. Scofield, Tables and Graphs of Atomic Subshell and Relaxation Data Derived from the LLNL Evaluated Atomic Data Library (EADL), Z=1-100, Technical Report UCRL-ID-50400.

[25] F. Salvat, J. M. Fernández-Varea, J. Sempau, PENELOPE-2014: A code System for Monte Carlo Simulation of Electron and Photon Transport, OECD/NEA Data Bank, Issy-les-Moulineaux, France, 2014. Available in PDF format from http://www.nea.fr/lists/penelope.html.

[26] R. P. Brent, Algorithms for Minimization without Derivatives, Prentice Hall, 1973.